Journal of Mining and Earth Sciences

Website: https://jmes.humg.edu.vn

# Assessing coastal urbanization and land use efficiency from multi-temporal optical imagery using machine learning: case study in Ha Long City

Hung Manh Nguyen [1,2], Toan Duy Dao [3,*], Chieu Dinh Vu [3], Dung Ngoc Luong [3], Dong Thanh Khuc [3], Son Mai Le [1], Trong Gia Nguyen [4]

*[1] Vietnam National Space Center, Vietnam Academy of Science and Technology, Hanoi, Vietnam*

*[2]Graduate University of Science and Technology, Vietnam Academy of Science and Technology, Hanoi, Vietnam*

*[3] Faculty of Bridge and Road, Hanoi University of Civil Engineering, Hanoi, Vietnam*

*[4] Faculty of Geomatics and Land Administration, Hanoi University of Mining and Geology, Hanoi, Vietnam*

ARTICLE INFO

*Article history:*
Received 18th Jan. 2026
Revised 17th Apr. 2026
Accepted 02nd May 2026

*Keywords:*
Land-Use/Land-Cover (LULC),
Machine Learning,
Optical Satellite imagery,
Urbanization dynamics.

ABSTRACT

*Coastal cities are highly dynamic environments subject to intense pressures from urbanization, population growth, and environmental change, making spatiotemporal urban development analysis critical for sustainable planning. This study utilizes multi-temporal Landsat and Sentinel-2 imagery from 1995÷2025 to map land-use/land-cover (LULC) patterns and evaluate urban expansion in Ha Long City. A Random Forest classifier was applied using spectral features and key remote-sensing indices, including NDVI, NDBI, MNDWI, CMRI, and elevation data. Post-classification change detection was then conducted to identify major transitions from natural and agricultural surfaces to built-up areas. The classification results show high accuracy, particularly for built-up land, with F1-scores increasing from 0.88 in 1995 to 0.96-0.98 after 2010, indicating consistent producer's and user's accuracy for long-term monitoring. Over three decades, Ha Long's urban land expanded from about 2,097 ha to more than 7,188 ha, raising the regional urbanization level from 8.7% to nearly 30%. Urban growth predominantly extended toward coastal zones, bayfront areas, and major transportation corridors, accompanied by reductions in natural forests, mangroves, and water surfaces due to reclamation and spatial expansion. Analysis of urbanization speed and rate highlights contrasts between saturated urban cores and areas with remaining development capacity. Zones with high growth rates but low existing urban share represent potential growth clusters, while nearly saturated areas tend toward vertical development or outward expansion. These findings provide a scientific basis for land-use planning and sustainable urban development strategies in Ha Long City.*

Copyright © 2026 Hanoi University of Mining and Geology. All rights reserved.

*Corresponding author
*E-mail:* toandd@huce.edu.vn
DOI: 10.46326/JMES.2026.67(4).05

## 1. Introduction

Approximately 35÷40% of the global population lives within 100 km of coastlines, and around 10÷12% resides in low-lying coastal zones, which are particularly sensitive and highly vulnerable to heavy rainfall, storm surges, and sea-level rise (UN, 2011; Reimann et al., 2023). Coastal cities are engines of economic growth and socioeconomic development, yet they also face intensifying environmental and climate-related challenges. Rapid urbanization increases population density, asset concentration, and infrastructure exposure in high-risk zones susceptible to flooding, erosion, storm surges, and tidal inundation (Hinkel et al., 2014). Numerous studies have shown that coastal flooding in cities, in the absence of adequate adaptation measures, could cause annual economic losses amounting to a significant share of national GDP by the end of the 21st century, and the number of people exposed to this risk continues to rise as cities expand into coastal areas (Hinkel et al., 2014; Kirezci et al., 2023).

In Vietnam, major urban centers such as Ho Chi Minh City, Da Nang, Hai Phong, Can Tho, and coastal cities across the Mekong Delta play an important role in socio-economic development, yet they are also "hotspots" exposed to urban flooding, erosion, and saltwater intrusion (Vachaud et al., 2019; Cao et al., 2021; Nguyen et al., 2021; Xiao et al., 2021; Pham et al., 2023; Tran et al., 2024; WB, 2025). Population pressure and growing infrastructure demands have driven rapid urban expansion into low-lying areas and floodplains, thereby increasing the vulnerability of coastal zones (Do et al., 2025). Additionally, coastal urbanization, characterized by large-scale land reclamation to accommodate industrial, tourism, residential, transportation, and port-related development, has induced environmental and geomorphological transformations (Pham et al., 2025).

Coastal reclamation projects contribute to economic growth, but also alter shoreline movement, nearshore hydrodynamics, and sediment flows, resulting in shoreline erosion, sediment imbalance, and the degradation of mangroves, tidal flats, and seagrass beds, which are natural defensive buffers that shield coastlines from waves and storm surges (Do et al., 2025; Nguyen and Chinh, 2025; van Maren et al., 2025). The continued decline of such ecosystems may increase the risks of flooding and erosion, with long-term consequences for livelihoods, infrastructure, and the sustainable development of cities in low-lying coastal zones. Land reclamation and seaward urban expansion are accelerating in major Vietnamese urban areas such as Ha Long, Hai Phong, Da Nang, Nha Trang, and Can Gio, leading to significant impacts on topography, hydrological regimes, ecosystems, and regional climate resilience (Ngo et al., 2020; Duong et al., 2021; Do et al., 2025).

Consequently, the systematic identification, monitoring, and assessment of coastal urbanization has become increasingly urgent to improve spatial planning quality and support adaptive development strategies based on scientific evidence and quantitative data. Thus, many studies in Vietnam and elsewhere have examined urban expansion and flood risks in coastal regions to support urban monitoring, zoning adjustments, housing demand forecasts, and re-evaluation of tourism, port, and logistics potential. However, traditional approaches relying on field surveys and administrative statistics often remain fragmented across jurisdictions, costly to maintain, difficult to standardize over time, and limited in their capacity to provide continuous updates. As a result, they remain insufficient for long-term monitoring of urban dynamics at the spatial-temporal resolution required for effective planning and adaptation (Mishra et al., 2024).

Over the past two decades, advancements in remote sensing, artificial intelligence (AI), and big data have opened new avenues for urban studies (Zhu et al., 2017; Zhou and Weng, 2024). Remote sensing offers major advantages, including synoptic spatial coverage and short revisit cycles that enable continuous monitoring of urban dynamics. Long-term satellite archives such as Landsat and Sentinel offer temporal consistency, enabling reliable inter-period comparisons. In addition, cloud-computing platforms (e.g., Google Earth Engine) support large-scale data processing and reduce the cost of data acquisition compared with traditional approaches. Meanwhile, AI, particularly machine-learning (ML) and deep-learning (DL) models, has enhanced automated classification and change detection across multi-sensor imagery. It has also enhanced nonlinear feature learning and multi-source data fusion (optical, radar, DEM), while transfer learning and modern deep architectures further improve mapping accuracy and cross-regional generalization of urban models (Zhu et al., 2017; Ma et al., 2019). In urbanization studies, the combined use of remote sensing and AI can support several purposes, including (1) multi-temporal land use/land cover (LULC) mapping and change detection to quantify urban expansion; (2) inference of urban intensity and morphology (imperviousness, built-up structure, building height/volume) and detection of infrastructure footprints; (3) derivation of socio-economic indicators from night-time lights and spatial population distribution; (4) assessment of urban environmental and climatic conditions such as heat islands, green space, and air quality; (5) flood and subsidence modeling using integrated LULC/DEM and InSAR data; and (6) planning and governance tasks including land-use scenario comparison, monitoring of compliance and reclamation, and post-disaster recovery tracking (Rasul et al., 2017; Brown et al., 2022; Destefanis et al., 2025).

In Vietnam, the combination of remote sensing (RS) with AI/ML has increasingly become a critical approach for urban research and governance. In 2014, Landsat time series combined with DMSP-OLS night-time lights were used to map urban transitions in the Red River Delta (Castrence et al., 2014). This study represents one of the earliest applications of remote sensing and big data approaches in the country. In Hanoi, multi-temporal Landsat imagery and support vector machine (SVM) models have been applied to quantify built-up areas and spatial dynamics during the period 1993÷2010 (Nong et al., 2015). Subsequent studies developed time-series spatial metrics to characterize growth modes, such as infilling and edge expansion. These approaches have been used to analyze long-term peri-urbanization trends and monitor near-real-time expansion (Mauro, 2020; Dang et al., 2023). In Ho Chi Minh City, satellite data and cloud-based platforms have supported a wide range of urban analytics. These incluce tracing directional and temporal expansion using Landsat data from 1979÷2022 and Random Forest models for planning support (Goldblatt et al., 2018). Other studies have evaluated the performance of machine-learning algorithms, such as backpropagation neural network (BPNN), support vector machine (SVM), and random forest (RF), for urban land use/land cover classification using Landsat-8 imagery. Meanwhile, high-resolution remote sensing has been integrated with artificial neural networks (ANN) optimized by genetic algorithms to map flood susceptibility in Hanoi. The Geo-ML framework, including gradient boosting and deep neural networks, has been applied to simulate urban heat island patterns in Da Nang (Trinh and Bui, 2023). Similarly, RS-AI approaches have been employed in coastal cities such as Ha Long, Hai Phong, Hue, Da Nang, and Nha Trang (Vu et al., 2024; Do et al., 2025). In addition, multi-period LULC mapping has been widely conducted across Vietnamese cities for various applications. These studies demonstrate that RS and AI not only accelerate and standardize LULC and built-up mapping workflows, but also support analyses of urban morphology, long-term trends, and climate-related risks, thereby providing essential quantitative foundations for urban planning decisions in Vietnam's major cities.

Despite the rapid growth of RS-AI applications in urban research, several critical gaps remain underexplored. The perspective on seaward urbanization through land reclamation is still poorly examined. Most studies focus on onshore expansion while paying limited attention to land reclamation, reconstructing long-term, high-resolution urban change trajectories with cross-city comparability, and quantifying land-structure transitions together with indicators of construction intensity and morphology, providing direct inputs for risk assessment and adaptive planning. To address these gaps, this study combines multi-spectral, multi-temporal optical remote sensing data with machine-learning models to generate a time series of LULC maps. These maps characterize land-cover categories and their structural transitions over time. This enables the assessment of urbanization speed, trends, and land-structure change in a typical coastal city located in northern Vietnam over the past 30 years. Ha Long City was selected as the case study because of its rapid urbanization, extensive land reclamation, and intense land-use conversions along the coast. The results also support methodological validation and the derivation of indicators for urban planning and climate adaptation.

## 2. Study area and datasets

### *2.1. Study area*

Ha Long City, located at the center of Quang Ninh Province, is a coastal gateway urban area connecting the northern economic region with the Gulf of Tonkin. It borders Cam Pha to the east, Hoanh Bo (now incorporated into Ha Long City) to the north, Quang Yen to the west, and opens southward toward Ha Long Bay (Figure 1). The city has a distinctive two-shore urban structure, Hon Gai and Bai Chay, connected across Cua Luc Bay by the Bai Chay cable-stayed bridge, which forms the primary development axis. Ha Long is characterized by a marine karst landscape of limestone islands, supporting a development orientation focused on high-quality tourism and services integrated with conservation. Due to its strategic position at the gateway to the Red River Delta and within the Hanoi-Hai Phong-Quang Ninh growth triangle, Ha Long plays a central role as the province's administrative center, logistics hub, and key economic growth pole, supporting the transition from mining to services, clean industries, and the maritime economy (Vu et al., 2024).

Driven by growing demand for urban land and industrial, port, and logistics space, urban development has increased in Ha Long. Urban expansion has followed two main pathways: outward extension into foothill zones through terrain grading and leveling, and large-scale coastal reclamation since the early 2000s, which has converted water surfaces and tidal flats into buildable land (Vu et al., 2024; Do et al., 2025). This expansion has supported economic growth, but it has simultaneously reduced mangrove forests and tidal flats. In addition, it has altered shoreline configurations, tidal processes, and sediment regimes. These changes have increased the risks of flooding and placed greater pressure on drainage and environmental infrastructure. Rapid, project-based land conversion across multiple administrative levels has further limited the continuity and standardization of temporal datasets, making it difficult to reconstruct the long-term spatial trajectories of coastal urban development. Therefore, studying urbanization processes and land use/land cover transitions toward urban land in Ha Long is essential for quantifying the speed, direction, and structural patterns of change, including land reclamation. It also provides a based foundation for planning and climate adaptation.

### 2.2. Data used

In this study, we employed optical remote sensing imagery from Landsat (TM/OLI) and Sentinel-2 (MSI), together with the SRTM DEM, to generate LULC maps for analyzing the urbanization trajectory of Ha Long City. Landsat 5 TM and Landsat 8 OLI provide data across the VIS-NIR-SWIR spectrum at 30-m resolution, along with a 15-m panchromatic band (OLI) and a 100-m thermal band (TIRS) (https://landsat.gsfc. nasa.gov/ satellites/). With a 16-day revisit cycle and a continuous multi-decadal archive, Landsat serves as a base data source for long-term trend monitoring (Wulder et al., 2019; Vu et al., 2024). Meanwhile, Sentinel-2 offers 13 spectral bands, ranging from ultra-blue to SWIR at 10, 20, and 60 m resolutions,

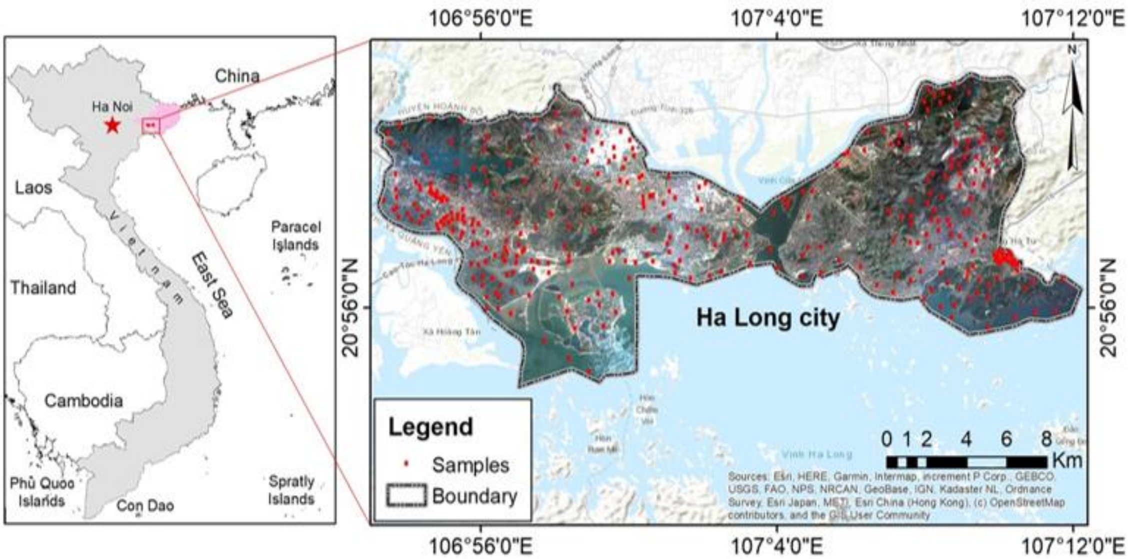


*Figure 1. The area of Ha Long City within the boundary in 2013.*

with a 5-day revisit cycle from the Sentinel-2A/B constellation (https://sentinels.copernicus.eu/copernicus/sentinel-2). Its spectral configuration is effective for distinguishing impervious surfaces, coastal vegetation, and detecting near-real-time changes. In addition, the SRTM DEM, with 1 arc-second (~30 m) resolution derived from radar interferometry, supports terrain correction and improves object classification in the hilly coastal landscape.

Data were acquired at five-year intervals from 1995÷2025. Landsat 5 and Landsat 8 imagery were used for 1995÷2015, while Sentinel-2 data were utilized for 2020 and 2025 (Table 1).

*Table 1. Satellite imagery datasets used.*

| No | Satellite & Sensor | Spatial resolution (m) | Acquisition Date | Data sources |
|---|---|---|---|---|
| 1 | Landsat 5 TM | 30 | 1995-11-24 | USGS |
| | | | 2000-12-23 | |
| | | | 2005-03-08 | |
| | | | 2010-11-01 | |
| 2 | Landsat 8 OLI | | 2015-01-15 | |
| 3 | Sentinel 2 MSI | 10 | 2020-12-06 | ESA |
| | | | 2025-03-20 | |
| 4 | SRTM | 30 | 2000 | USGS |

All scenes were selected during the dry season with cloud cover below 10%, and were processed using quality assessment (QA) bands for cloud and shadow masking to ensure stable spectral signatures and consistent image geometry. This selection approach reduces cloud-related noise and enhances the reliability of LULC classification, thereby improving coastal urbanization monitoring. Satellite imagery and DEM data were accessed and processed directly on the Google Earth Engine (GEE) platform.

## 3. Research methodology

To generate LULC maps of Ha Long, this study applies a consistent data-processing workflow consisting of the following steps: image preprocessing, computation of spectral indices, selection of training samples, algorithm selection and model training, classification, accuracy assessment, post-classification processing, LULC map production, and compilation of statistical summaries for each period. All processing tasks were implemented through GEE, with data visualization performed using ArcGIS software. Figure 2 illustrates the methodological framework employed to achieve objectives. The procedures for data preprocessing and spectral index calculation are presented in later sections.

### *3.1. Data preprocessing and spectral index computation*

This study uses Landsat Level-2 and Sentinel-2 Level-2A imagery, both corrected to surface reflectance. Before computing spectral indices, the imagery was preprocessed through two steps: (1)

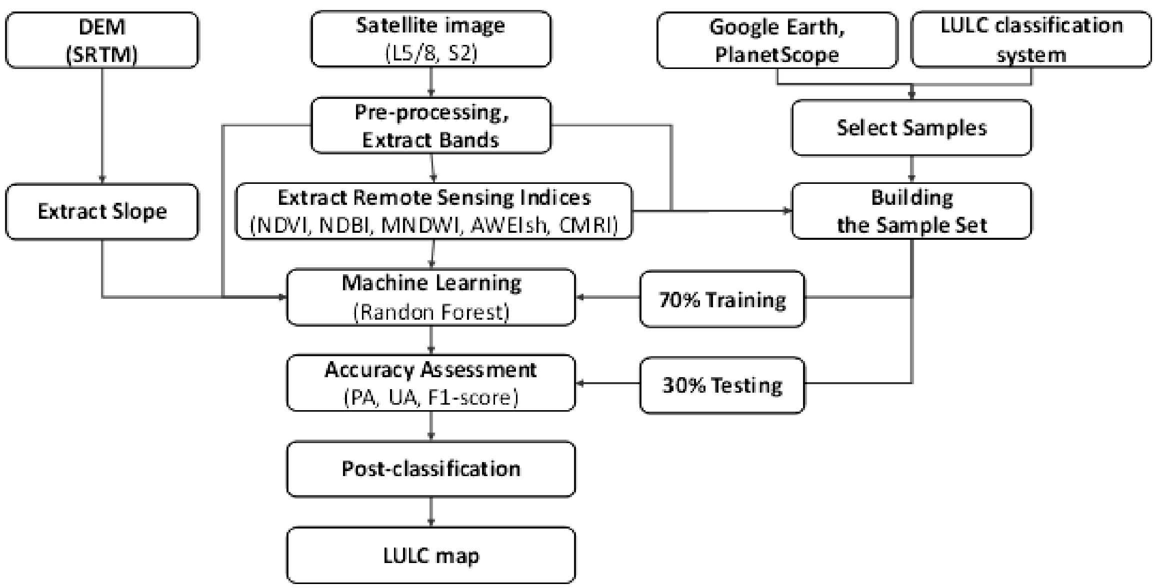


*Figure 2. Workflow for LULC classification.*

cloud and shadow masking using quality bands (QA_PIXEL/QA_RADSAT for Landsat, SCL/QA60 for Sentinel-2), and (2) brightness balancing (or histogram matching) to reduce illumination differences across scenes. The DEM was utilized to derive slope and provide topographic information supporting land-cover classification in hilly coastal areas. Terrain variables also helped reduce topography-related spectral variability and account for illumination differences.

For land-cover classification, spectral indices enable rapid identification of key coastal-urban features without field surveys, ensuring processing efficiency and temporal consistency. Among numerous indices proposed in the literature, several are especially useful for major surface groups. Normalized Difference Vegetation Index (NDVI) identifies and tracks green spaces, including urban parks, roadside vegetation, and coastal green belts, allowing seasonal and interannual vegetation monitoring (Rouse, 1973). Modified Normalized Difference Water Index (MNDWI) enhances open water features in urban areas, clearly delineating hydrological elements such as channels, lagoons, retention lakes, while monitoring changes caused by seasonal variation or land reclamation, and post-rainfall waterlogging (Xu, 2006). In coastal bay environments where shadows from mountains or high-rise buildings are common, the Automated Water Extraction Index-shadow (AWEIsh) maintains high sensitivity to water surfaces, improving the reliability of water-mask generation for reclaimed and port zones (Feyisa et al., 2014). Alongside vegetation and water indicators, Normalized Difference Built-up Index (NDBI) highlights impervious and built-up surfaces, enabling detection of development hotspots and estimation of urban compactness (Zha et al., 2003). For coastal ecosystems, the Combined Mangrove Recognition Index (CMRI) distinguishes mangrove forests from tidal flats and saltmarshes, allowing monitoring of mangrove loss and recovery (Gupta et al., 2018). The formulas for calculating spectral indices are presented as follows:

$$NDVI = \frac{NIR - Red}{NIR + Red} \quad (1)$$

$$MNDWI = \frac{Green - SWIR1}{Green + SWIR1} \quad (2)$$

$$AWEIsh = Blue + 2.5 * Green - 1.5 * (NIR + SWIR1) - 0.25 * SWIR2 \quad (3)$$

$$NDBI = \frac{(SWIR - NIR)}{(SWIR + NIR)} \quad (4)$$

$$CMRI = NDVI - MNDWI = \frac{(NIR + SWIR1) - (Red + Green)}{(NIR + SWIR1) + (Red + Green)} \quad (5)$$

Where, Red, Green, and Blue refer to the red, green, and blue portions of the electromagnetic spectrum, respectively. NIR stands for Near Infrared, while SWIR1 and SWIR2 denote Shortwave Infrared bands at different wavelength ranges.

When integrated into threshold-based or ML classification, these indices allow the extracting of vegetation patterns, water, and built-up areas, and the assessment of land reclamation dynamics, associated flood and heat risks.

### *3.2. Land-cover classification system and sampling strategy*

For a coastal city such as Ha Long, the study establishes a seven-class LULC schema tailored to regional characteristics and satellite spatial resolution. The classes include: Built-up land (BU), Water (W), Forest (F), Coal mine land (CM), Agriculture (A), Bare soil (BS), and Mangrove forest (MF). Detailed identification criteria for each class are provided in Table 2. Training samples were collected through visual interpretation of PlanetScope satellite imagery supported by high-resolution images from Google Earth Pro. Sample points were taken at the centroids of polygons delineated over homogeneous land cover areas and were further checked using spectral indices to ensure sample reliability. Built-up samples were selected from urban and industrial areas and verified using high NDBI values. Water samples were collected from the central parts of estuaries, lakes, and offshore areas and validated using both high MNDWI and AWEIsh values. Forest samples were obtained from dense canopy areas, with preference given to protected forests, and confirmed using high NDVI values. Coal mine samples were delineated around open-pit mining areas in known mining regions.

*Table 2. Characteristics and number of training samples across years.*

| LULC | Number of Sample Points/Polygons | | | | | | | Description |
|---|---|---|---|---|---|---|---|---|
| | 1995 | 2000 | 2005 | 2010 | 2015 | 2020 | 2025 | |
| BU | 50/3 | 50/3 | 50/3 | 50/2 | 50/2 | 50/3 | 50/3 | Areas that are built-up or under construction |
| W | 50/5 | 50/5 | 50/5 | 50/5 | 50/1 | 50/0 | 50/0 | Surface water of canals, rivers, streams, ports, estuaries, and coastal waters |
| F | 49/4 | 49/4 | 50/3 | 50/3 | 50/3 | 50/2 | 50/2 | Includes natural forests and plantation forests |
| CM | 48/1 | 48/1 | 48/1 | 48/1 | 50/1 | 48/0 | 48/0 | Coal-mining land |
| A | 50/1 | 50/1 | 50/1 | 50/1 | 50/1 | 50/0 | 50/0 | Includes perennial cropland, annual cropland, and rice paddies |
| BS | 50/3 | 50/3 | 50/3 | 50/2 | 50/2 | 50/0 | 50/0 | Uncultivated or abandoned land |
| MF | 50/2 | 50/2 | 50/2 | 50/2 | 50/2 | 50/0 | 50/0 | Mangrove forest land |
| Total samples | 682 | 666 | 644 | 761 | 729 | 756 | 741 | |

Agricultural samples were selected from cropland and rice paddies and verified using multi-temporal imagery to confirm seasonal cultivation patterns. Bare soil samples were collected from construction sites, sandbars, and unused land and visually inspected to exclude impervious surfaces. Mangrove samples were selected from tidal coastal and estuarine areas and verified using high-resolution imagery, with limited confusion with aquatic vegetation considered acceptable for model training.

Training data were organized as spatial objects, with each point or polygon assigned a class label and attribute fields used for model training. Samples for the seven time periods were digitized in GEE, and cross-checked using Google Earth and available high-resolution optical data. The distribution and number of samples by class and year are summarized in Table 2, and sampling locations are shown in Figure 1.

The sampling dataset was divided into two parts, with 70% used for training and 30% for validation of the machine-learning model. The split was performed using stratified random sampling by LULC class and year to ensure that all classes were well represented in both subsets. Validation samples were kept spatially separate from training samples to reduce spatial autocorrelation and better reflect the model's ability to generalize. A fixed random seed was applied to ensure reproducibility. Model performance was assessed using confusion matrix and standard accuracy metrics, including User's Accuracy (UA), Producer's Accuracy (PA), the F1-score, and area-adjusted accuracy with 95% confidence intervals.

### 3.3. Random forest algorithm

Random Forest (RF) is an ensemble machine-learning algorithm constructed from multiple decision trees, generated via bootstrap aggregation (bagging) and random feature selection at each split. Classification is based on majority voting. This design reduces inter-tree correlation, limits overfitting, enables estimation of out-of-bag error, and provides measures of variable importance, making RF robust to noise and spectral variability in remote-sensing data (Breiman, 2001). In LULC classification, numerous studies show that RF achieves high and stable accuracy. It performs well in high-dimensional feature spaces, captures nonlinear relationships, and requires relatively limited hyperparameter tuning compared with SVM or DL models when training data are limited. RF offers several advantages, including strong performance, effectiveness with heterogeneous and nonlinear datasets, and the ability to produce class probabilities for uncertainty mapping. Nonetheless, the method has some limitations, such as lower interpretability than linear models, potential bias in Gini-based variable importance if not controlled, sensitivity to class imbalance, and the risk of spatial leakage when spatial blocking is not applied during validation. These issues can be mitigated through class weighting, spatial blocking strategies, and the reporting of class-wise accuracy metrics (Belgiu and Drăguţ, 2016).

RF is widely implemented across geospatial platforms, including Google Earth Engine, scikit-learn, R, and ArcGIS Pro. It can also be efficiently deployed at scale using cloud-based batch processing. Given the multi-band spectral data and indices (NDVI, MNDWI, AWEIsh, NDBI, CMRI), together with terrain variables (DEM, slope), RF is well suited for LULC classification. It effectively integrates multi-source information and yields spatially and temporally consistent results, particularly when applied to Landsat and Sentinel image series.

### 3.4. Accuracy assessment

Accuracy for each class is quantified using Producer's Accuracy (PA) and User's Accuracy (UA), with overall performance summarized by the F1-score. PA reflects how completely reference samples of a class are correctly retrieved, and high PA indicates low omission error. UA measures the reliability of each mapped class, and high UA indicates low commission error (Foody, 2002). To balance completeness (PA) and correctness (UA) under class imbalance, both class-wise F1-scores and the weighted F1-score are computed to represent overall model performance independent of sample distribution (Goutte and Gaussier, 2005). Furthermore, UA, PA, and F1 are adopted as the primary accuracy metrics in place of the Kappa coefficient, consistent with recent critiques in the remote-sensing literature (Foody, 2020). This approach provides a transparent, class-specific assessment of omission and commission errors, while enabling reliable comparisons across years and among different feature configurations.

### 3.5. Post-classification

Following LULC classification, the raster output often contains salt-and-pepper noise, including isolated pixels or small patches inconsistent with the surrounding land cover. To address this, spatial filtering methods such as 3×3 or 5×5 majority filtering, morphological opening and closing, and minimum mapping unit rules are applied to remove or merge small clusters, smooth boundaries, and reduce local misclassifications. The filtered rasters are then converted to vector format to support noise removal (e.g., offshore vessels) and to facilitate area calculation and statistical analysis. Vector layers may be dissolved by class, cleaned of sliver polygons, checked for topology, and merged or separated according to cartographic rules. Vector data also allow accurate area computation, aggregation by administrative units (e.g., wards, communes, coastal belts), and consistent cross-year comparisons.

Through this sequence of filtering, raster-to-vector conversion, and topological refinement, the post-processed LULC maps become more stable and interpretable. They meet the requirements for area reporting, change analysis, and downstream applications such as flood modeling, spatial planning, and coastal-reclamation monitoring.

## 4. Results and discussions

### 4.1. Maps of LULC classification

The LULC maps of Ha Long City from 1995 to 2025, presented in Figure 3, illustrate substantial changes in land use and surface cover over three decades. These results support the identification of long-term spatial transition patterns, thereby enabling assessments of urbanization expansion, economic activities, and resource exploitation. The time-series mapping framework enables visually track landscape change and serves as a reference for urban planning and resource management.

The results in Figure 4 indicate a pronounced trajectory of urban expansion over the study period. In 1995, the landscape was dominated by forests and natural vegetation, widely distributed across the eastern and western parts of the city, while built-up areas were concentrated around the urban core and along major transport corridors, particularly National Highway 18. By 2000, and more clearly by 2005, built-up areas expanded along the bayfront and national highway, reflecting rapid economic growth and tourism development following the completion of the Bai Chay Bridge, which connected the two sides of Cua Luc Bay. By 2010, urbanization accelerated, with built-up areas encroaching on former agricultural and bare-soil land. Residential zones formed predominantly along the eastern coastline and within the transitional area between the two urban sectors, resulting in a more continuous and less fragmented development pattern.

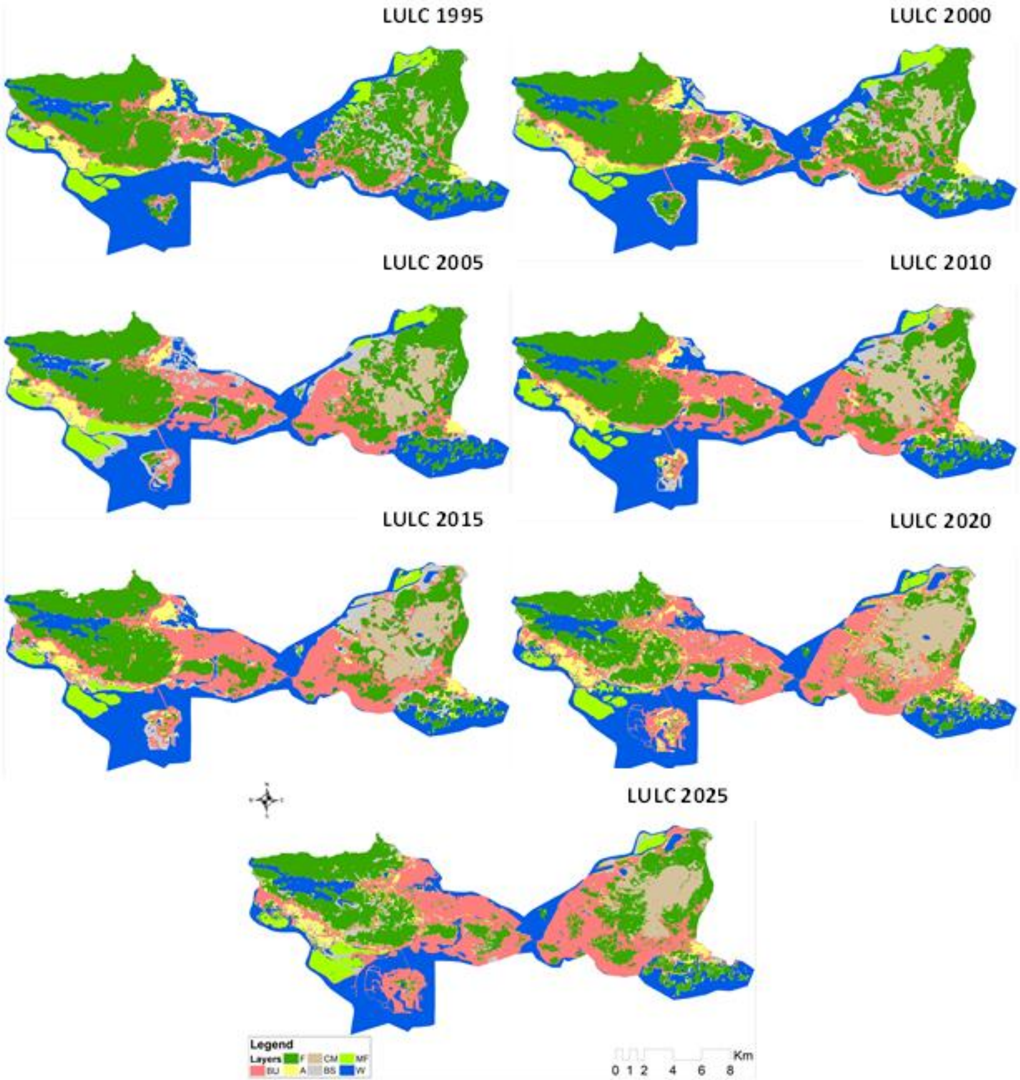


*Figure 3. The dymanics of Ha Long's land cover over 30 years.*

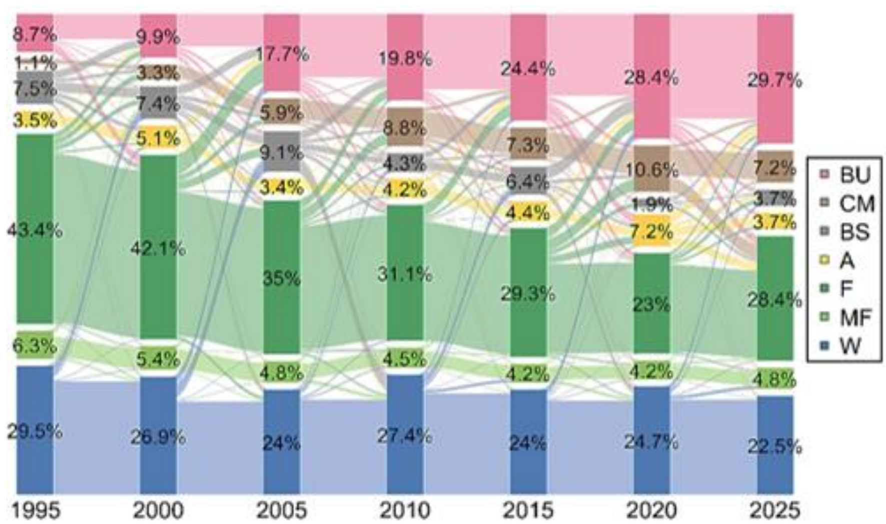


*Figure 4. Changes in the proportion of land-use and LULC classes in the study area from 1995÷2025.*

Between 2015 and 2020, landscape change intensified, with new urban areas and infrastructure extending seaward and expanding toward the southwest. Forest cover became more fragmented, and agricultural land declined sharply in central and coastal zones. By 2025, urbanization remained rapid, with higher construction density and continued losses of natural land cover. This resulted in a more spatially cohesive urban structure but lower landscape diversity.

Over the past three decades, the spatial composition of land cover in Ha Long has shifted markedly toward urban functions. Built-up areas expanded steadily and emerged as the dominant land category, while forested and vegetated surfaces experienced declines in both area and spatial continuity. Agricultural land was progressively converted to urban and specialized uses. Bare soil and tidal flats were extensively reclaimed or infilled to accommodate infrastructure projects. Water surfaces decreased, mainly driven by coastal development projects. The 2025 LULC map indicates this trend, with expansion of urban and service-related areas into production forest, nearshore bare land, and mangrove forest areas. The LULC time series demonstrates that urbanization in Ha Long has been both intense and continuous over three decades. Built-up land has expanded alongside the contraction and fragmentation of natural and agricultural areas. These changes reflect pressures from economic growth, tourism development, and infrastructure expansion on the urban landscape. The findings provide valuable visual and quantitative evidence to support sustainable development planning and to inform effective land-use management strategies in the future.

### 4.2. Accuracy assessment

The classification accuracy for the study area is summarized in Table 3. The results show that the water (W) and forest (F) classes achieved consistently high and stable accuracy throughout the 1995-2025 period. Both classes exhibit PA and UA values approaching 0.99÷1.00, with F1-scores in the range of 0.99÷1.00. These two classes are readily identifiable due to their distinctive spectral signatures, such as strong NIR/SWIR absorption for water and high NIR reflectance for vegetation.

The built-up (BU) class maintains high and relatively stable performance. The F1-score increases from 0.88 in 1995 to 0.96÷0.98 during the 2010÷2025 period. This improvement aligns with the inclusion of NDBI and the higher spatial resolution of recent imagery.

*Table 3. Accuracy assessment results for land-cover classification.*

| Content | Class | 1995 | 2000 | 2005 | 2010 | 2015 | 2020 | 2025 |
|---|---|---|---|---|---|---|---|---|
| PA | BU | 0.88 | 0.87 | 0.97 | 0.95 | 0.93 | 1 | 0.98 |
| | W | 1 | 1 | 0.99 | 1 | 1 | 1 | 1 |
| | F | 0.99 | 0.99 | 0.99 | 1 | 1 | 1 | 1 |
| | CM | 0.86 | 0.69 | 0.72 | 0.83 | 0.96 | 0.98 | 0.82 |
| | A | 0.93 | 0.92 | 0.92 | 1 | 0.95 | 0.97 | 0.97 |
| | MF | 0.91 | 1 | 0.95 | 0.95 | 1.00 | 0.90 | 0.86 |
| | BS | 0.92 | 0.94 | 0.92 | 0.87 | 0.98 | 0.72 | 0.80 |
| UA | BU | 0.90 | 0.95 | 0.95 | 0.98 | 0.98 | 0.96 | 0.97 |
| | W | 0.99 | 1 | 0.99 | 0.99 | 1 | 0.97 | 0.95 |
| | F | 0.97 | 0.93 | 0.93 | 0.99 | 1 | 1 | 0.97 |
| | CM | 1 | 0.92 | 1 | 1 | 1 | 1 | 0.94 |
| | A | 1 | 0.79 | 1 | 1 | 1 | 0.97 | 0.97 |
| | MF | 0.95 | 1 | 1 | 1 | 0.95 | 0.97 | 0.97 |
| | BS | 0.90 | 0.96 | 0.93 | 0.92 | 0.92 | 0.96 | 0.83 |
| F1-score | BU | 0.88 | 0.91 | 0.96 | 0.96 | 0.95 | 0.98 | 0.97 |
| | W | 1 | 1 | 0.99 | 0.99 | 1 | 0.99 | 0.97 |
| | F | 0.98 | 0.96 | 0.96 | 1 | 1 | 1 | 0.99 |
| | CM | 0.93 | 0.79 | 0.84 | 0.91 | 0.98 | 0.99 | 0.89 |
| | A | 1 | 0.85 | 0.96 | 1 | 0.97 | 0.97 | 0.97 |
| | MF | 0.93 | 1 | 0.98 | 0.97 | 0.97 | 0.94 | 0.91 |
| | BS | 0.91 | 0.95 | 0.92 | 0.89 | 0.95 | 0.83 | 0.81 |

The agriculture (A) class generally performs well, except in 2000, when UA decreases to 0.79, resulting in an F1-score of 0.85. This decline is likely associated with seasonal variability or wet soil conditions that cause confusion with shallow water or bare soil. In all other years, F1-scores range between 0.96 and 1.00.

The coal-mine (CM) class shows the greatest variability. PA is lower in 2000÷2005 (0.69÷0.72) and again in 2025 (0.82), with corresponding decreases in F1-scores (0.79÷0.84 and 0.89). This pattern reflects rapid changes in mining surfaces (e.g., wet slurry and spoil heaps) and differences in sensor characteristics across the time series.

Mangrove forest (MF) classification remains strong up to 2015, with F1-scores of 0.97÷1.00, but declines after 2020 (from 0.94÷0.91) as PA decreases (from 0.90÷0.86). This drop suggests omission errors where mangrove patches are misclassified as tidal flats or saltmarsh vegetation.

Bare soil (BS) remains relatively stable, although PA decreases in 2010 (0.87) and 2020 (0.72), leading to lower F1-scores (0.89 and 0.83÷0.81). These declines reflect confusion between BS and BU or CM in areas undergoing land reclamation, construction, and spoil disposal. BS can also be confused with sandy coastal flats under low tidal conditions and with exposed lakebeds during dry or drought periods.

Results show that the RF model exhibits robust classification performance for the stable classes (W, F, and BU) and maintains acceptable accuracy for the more dynamic classes (A, MF, BS, and CM). Classification accuracy for these dynamic classes can be further improved by incorporating red-edge bands from Sentinel-2, NDMI, and GLCM-based texture metrics. Additional improvements can be achieved by increasing stratified sampling in challenging areas such as tidal flats, spoil heaps, and reclaimed land. Slope information may also be useful for CM, MF, and BS. Additional improvements may result from dry-season normalization and harmonization of Landsat and Sentinel-2 imagery. Post-classification filtering, minimum mapping unit (MMU) rules, and temporal consistency checks can reduce class-switching noise.

The classification results satisfied the requirements for multi-period urbanization monitoring. The built-up class exhibits consistently high and stable performance across all years, providing a reliable basis for analyzing the trajectory, intensity, and directional patterns of urban expansion. Reference classes such as water and forest further enhance model stability because of their distinct spectral signatures. In contrast, more complex classes like coal-mine, bare soil, and mangrove forest highlight characteristic confusion patterns, indicating areas where future improvement is needed. Incorporating texture features, moisture-related indices, and spatiotemporal constraints is expected to improve PA and F1-scores for these classess without altering the overall conclusions. Overall, the LULC classification results are sufficiently reliable for phase-by-phase urbanization analysis and support land-use planning and decision-making within the study area.

### 4.3. Discussions

#### 4.3.1. Area and proportion of land-cover types

Table 4 presents the areas of land-cover and land-use categories in the study area from 1995 to 2025. It provides a comprehensive overview of changes across seven land-use groups, including built-up land, coal-mine land, bare soil, agricultural land, natural forest, mangrove forest, and water bodies. This long-term dataset captures the main land-use transitions driven by urbanization, population growth, economic development, and natural processes over the past three decades.

*Table 4. Area of LULC classes in the study area, 1995÷2025 (unit in ha).*

| LULC\Year | 1995 | 2000 | 2005 | 2010 | 2015 | 2020 | 2025 |
|---|---|---|---|---|---|---|---|
| BU | 2097.4 | 2397.4 | 4298.2 | 4787.2 | 5911.5 | 6892.2 | 7188.3 |
| CM | 264.6 | 804.0 | 1418.4 | 2124.1 | 1760.5 | 2559.5 | 1744.1 |
| BS | 1825.5 | 1804.7 | 2205.0 | 1044.4 | 1543.3 | 472.2 | 897.7 |
| A | 856.6 | 1225.6 | 833.1 | 1020.4 | 1069.3 | 1734.6 | 893.3 |
| F | 10541.8 | 10220.7 | 8520.8 | 7569.5 | 7103.8 | 5596.0 | 6912.1 |
| MF | 1526.5 | 1297.5 | 1169.6 | 1079.6 | 1022.6 | 1019.9 | 1164.3 |
| W | 7157.8 | 6525.2 | 5827.1 | 6648.4 | 5828.9 | 6002.8 | 5477.6 |

Table 4 shows that built-up land has increased rapidly and continuously over the study period, expanding from 2,097.4 ha in 1995 to 7,188.3 ha in 2025. This growth reflects sustained urbanization and extensive infrastructure development. Land associated with mineral extraction exhibited notable fluctuations, peaking in 2020 before declining in 2025. This pattern suggests adjustments associated with different planning phases. By contrast, bare soil shows strong variability, dropping sharply to 472.2 ha in 2020 as these areas were converted to built-up and specialized land uses, followed by a slight rebound in 2025.

Agricultural land shows irregular fluctuations, indicating flexible transitions between land-use purposes. Meanwhile, natural forest area decreases significantly from 10,541.8 ha to its lowest level in 2020 of 5596.0 ha, before increasing again in 2025. This change is likely linked to a combination of land-use conversion, logging from planted forest, and subsequent restoration efforts. The area of mangrove forest shows a gradual decline through 2020 but recovers slightly by 2025, suggesting the influence of conservation or rehabilitation initiatives. Water bodies show a general decline over time, associated with land reclamation, and infrastructure expansion.

The dataset reveals substantial shifts among land-use categories, marked by the expansion of built-up land and the decline of natural land types. These patterns reflect ongoing urbanization and spatial restructuring that have shaped land-use dynamics in the study area over the past three decades.

*4.3.2. Dynamics and transitions of land-cover types*

To clarify land-cover transitions across periods, Figure 4 illustrates the LULC changes from 1995 to 2025. The results show that urbanization has progressed continuously and intensively over the past three decades. Built-up land increased steadily, rising from 8.7% in 1995 to nearly 30% by 2025. This rapid upward trend reflects the pace of urban spatial expansion, particularly after 2000. The pattern is consistent with findings by Jalilov et al. (2021), who reported that urban land consumption in Ha Long City accelerated significantly after 2000 and far exceeded population growth. This agreement demonstrates that the LULC analysis in this study accurately captures the urban development pressures observable in the Landsat record.

Alongside the growth of built-up land, specialized-use land also expanded substantially during 2000-2020 before slightly declining in 2025. This pattern aligns with periods of intensive investment in infrastructure, tourism, ports, and industrial zones documented by (Jalilov et al., 2021). Their study noted that industrial and service development since the late 1990s drove the rapid expansion of functional zones and the large-scale conversion of agricultural and forest land to construction land. During this period, a distinctive conversion pathway emerged, in which forest land was replaced by residential land, mining areas, and bare soil, especially around 2020 when coal extraction and surface clearing were widespread. The observed pattern corresponds to the trajectory shown for 1995-2005 in Figure 4, where both built-up and specialized-use land increased while forest and other natural land declined.

By comparison, natural land covers such as forest, mangrove forest, and water bodies show an overall declining trend. Natural forest area decreased markedly from 1995 to 2020, reflecting the gradual loss of ecological space due to residential expansion, mining activities, and infrastructure development. Similar declines in mangrove and natural vegetation have been reported for Ha Long under increasing urban and industrial pressures (Jalilov et al., 2021; Vu et al., 2024). Although the chart shows a modest recovery in 2025, forest extent remains significantly lower than in the baseline year. Meanwhile, water area changes slightly reflect land reclamation during 1995-2005, particularly in Cua Luc Bay, where infrastructure and port development led to shoreline infilling. Moreover, built-up land growth shows clear spatial and temporal variation, with the most rapid increases occurring after 2010. This finding is consistent with the results reported by (Vu et al., 2024), who identified the fastest urban expansion during 2005-2010 and 2015-2020 (Figure 4). Between 2010 and 2020, urban expansion toward Ha Long Bay and the Tuan Chau Peninsula corresponded to the reduction in water area and the rise of coastal urban zones. This phase was characterized by extensive land reclamation for tourism services and marina infrastructure.

Coal mine land exhibits distinctive variations and plays a key role in land-use transitions in Ha Long. Its proportion increased sharply from 1995 to 2020, reflecting the expansion of open-pit mines, spoil heaps, and mining infrastructure in areas such as Ha Tu, Ha Khanh, Ha Phong, and Coc Sau. This expansion is closely linked to the conversion of forest land into mining areas and subsequently into bare land, a process that intensified before 2020. The growth of CM occurred alongside declines in forest and vegetation cover, demonstrating the influence of mining activities on landscape structure. This result is consistent with earlier findings by Nguyen et al. (Nguyen et al., 1999), who reported significant losses of forest and natural land due to coal exploitation in the late 1990s. Although the CM area decreases slightly by 2025, indicating partial mine closure, it remains a major driver of land-use restructuring in Ha Long. Other land-cover types, such as agricultural land and mangrove forest, display non-linear changes influenced by urban development. Agricultural land varies by development phase, reflecting flexible transitions driven by infrastructure and tourism demand, while mangrove forest declines through 2020 and recovers slightly by 2025. Water bodies gradually decrease over time, coinciding with land reclamation both within Cua Luc Bay during 1995-2005 and around Ha Long-Tuan Chau during 2010-2020. These trends illustrate the cumulative impacts of land reclamation and coastal urban development on the regional landscape.

The land-cover transition patterns from 1995 to 2025 reveal a clear urbanization trajectory marked by the expansion of built-up and specialized-use land and the simultaneous contraction of natural land covers. These patterns are consistent with findings from earlier studies of Ha Long, reinforcing the reliability of the results and clarifying the spatial context of urban development in the region.

Figure 5 illustrates the spatial patterns of land-cover transitions in the study area across the seven time periods from 1995 to 2025. The overlaid color layers highlight both the location and intensity of land-use changes, showing the progression of urbanization, land reclamation, and land-use conversion. Darker tones toward 2025 indicate continued expansion of developed areas and the spatial spread of urban growth.

Areas showing built-up transitions in Figure 5 indicate pronounced urban expansion, concentrated along coastal zones, bayfront areas, and major transportation corridors. This spatial pattern demonstrates that urbanization in Ha Long has progressed outward from the city center toward peripheral areas over nearly three decades. During 1995-2005, BU transitions appeared at low intensity, mainly around Cua Luc Bay and the Bai Chay area, where early land reclamation, site

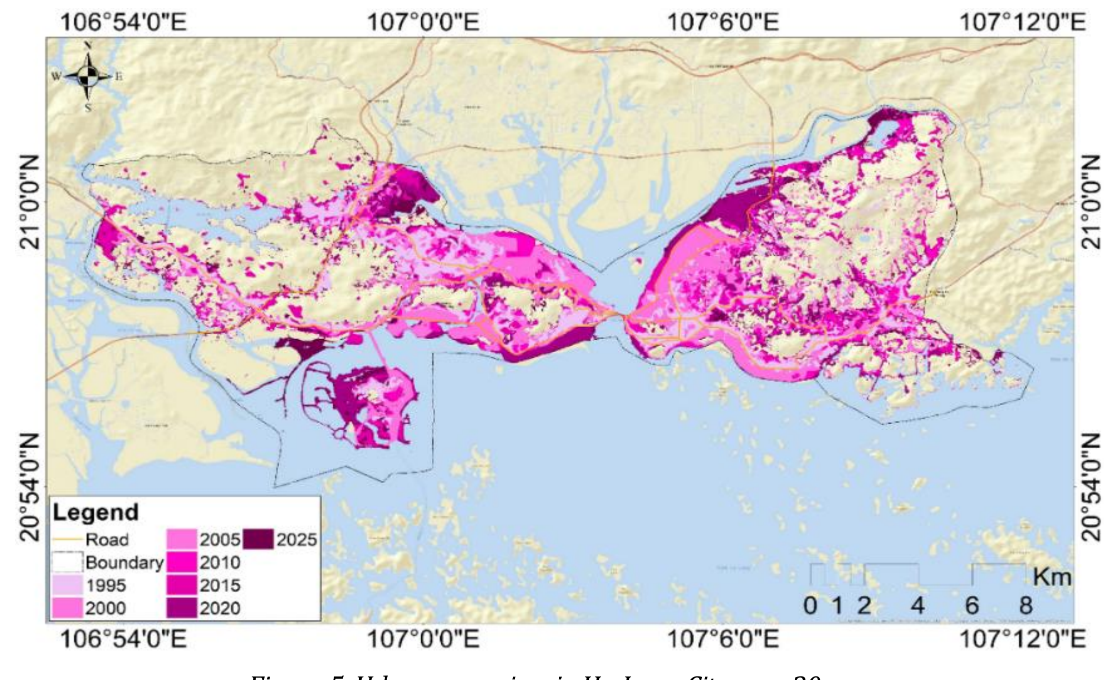


*Figure 5. Urban expansion in Ha Long City over 30 years.*

preparation, and tourism development first emerged. This period marks the onset of strong economic growth in Ha Long and the emergence of initial clusters of built-up conversion from agricultural land, bare soil, and tidal flats. These trends are consistent with (Nguyen et al., 1999), who documented increasing economic development pressure in the late 1990s and its early impacts on urban spatial structure.

From 2010 to 2020, both the extent and density of new built-up areas increased markedly. Urban expansion spread toward Ha Long Bay, the Tuan Chau Peninsula, and newly developed zones in Ha Khanh, Ha Trung, Bai Chay, and Viet Hung wards. Darker patches during this period reflect a faster and more spatially extensive phase of urban growth compared to earlier years. This pattern aligns with findings by Vu et al. (2024), who identified 2010-2020 as the most intensive period of urban expansion, concentrated along coastal corridors, leveled mountainous terrain, and major tourism and service nodes.

The map also reveals a clear pattern of seaward expansion of built-up areas. During the early phase (1995-2005), reclamation-related development was confined to Cua Luc Bay, where industrial facilities, ports, and tourism infrastructure were first established. In contrast, the 2010-2020 period is characterized by rapid urban growth on newly reclaimed land extending toward Bai Chay, Hung Thang, Gieng Day, and particularly the Tuan Chau Peninsula. This shift marks a move away from compact inner-city growth toward a bayfront and coastal development model, consistent with Ha Long's emphasis on tourism and service-based activities.

Overall, built-up expansion in Ha Long is uneven in space but follows a recognizable structure. Development concentrates along the coastline and national highway, advances onto reclaimed areas, and diffuses gradually across bayfront zones. This spatial configuration accurately reflects the urbanization trajectory of Ha Long over the past thirty years and is consistent with previous studies on the city's spatial development dynamics.

### 4.3.3. Urbanization rate and intensity

To assess the expansion of urbanization in Ha Long, the rate and intensity of urbanization were computed and presented in Figure 6. The urbanization-rate map identifies hotspots of land-use conversion, while the urbanization-intensity map distinguishes areas approaching land-capacity saturation from those with remaining potential for expansion. Both indicators, shown in Figure 6, are presented on a 500×500 m grid, allowing detailed analysis of spatial variation in the pace and extent of urbanization, and enhancing analytical capacity to interpret underlying development patterns.

In Figure 6a, red-orange cells indicate zones of high urbanization intensity, with many locations approaching 100%. These areas are concentrated in central Ha Long, along major transportation corridors, coastal roads, and at the interfaces of residential clusters. Such areas represent zones where buildable land is almost fully utilized, and open space has largely been converted to housing, commercial and service functions, or technical infrastructure. In contrast, dark-blue cells represent

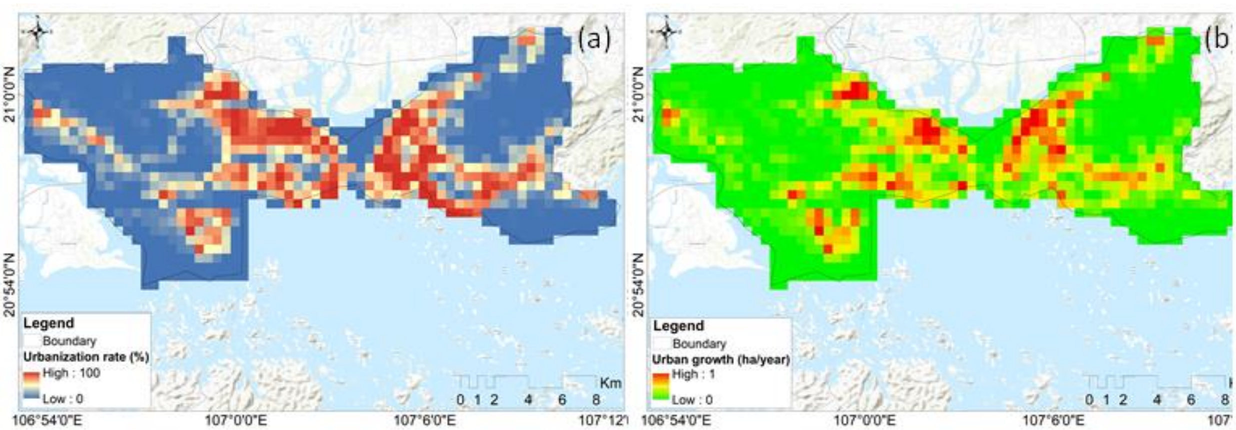


*Figure 6. Spatial distribution of the urbanizaion ratio (a) and urban growth rate (b) in Ha Long City over 30 years.*

areas with low urbanization, mainly found in peri-urban zones, mountainous terrain, or locations distant from primary road networks. These areas retain substantial land reserves and therefore offer considerable potential for urban development under suitable planning strategies or when investment projects are implemented.

Figure 6b illustrates the rate at which land has been converted to urban uses over the study period. Areas with high urbanization speed (shown in yellow-red) are concentrated along emerging development corridors, newly constructed or upgraded transportation routes, and the vicinity of expanding urban zones. Several locations with rapid increases overlap with areas that already exhibit high urbanization intensity, indicating ongoing infill development and increasing construction density within the urban core. Notably, some rapid urbanization zones occur in areas where the level of urbanization development remains low. This pattern is evident in the northern and northeastern parts of Cua Luc Bay, the southeastern coastal margin of Ha Long Bay, and the western corridor extending toward Hai Phong along the Ha Long-Hai Phong Expressway. These areas function as emerging growth fronts with high development potential and are likely to become centers of future urbanization.

The results indicate outward urban expansion from the existing urban core toward peripheral areas, particularly around Cua Luc Bay, along the southern axis toward Ha Long Bay, and westward toward Hai Phong City. This spatial pattern aligns with the region's multi-nodal urban development orientation. Based on the distribution of urbanization rate and intensity, future growth is likely to continue along major transportation corridors, coastal areas, commercial and service nodes, especially where strategic infrastructure investment is concentrated. Current hotspots of urbanization may develop into new urban centers or form continuous corridors as surrounding cells increase in density. Meanwhile, areas that remain open and are located near growth nodes are also expected to become transition zones in the coming years. By contrast, mountainous terrain and locations distant from primary infrastructure networks tend to maintain low development intensity unless influenced by large-scale investment.

## 5. Conclusions

The study results highlight the effectiveness of integrating multi-temporal remote sensing data with machine-learning models for land use/land cover classification, particularly in identifying built-up areas. The built-up class achieved consistently high and stable accuracy throughout the study period, with the F1-score increasing from 0.88 in 1995 to 0.96÷0.98 during 2010-2025. This improvement is supported by high Producer's and User's Accuracy values, demonstrating the capability of the Random Forest model to capture urban surfaces under complex spectral conditions and increasing development density. The robust performance of the built-up class provides a reliable basis for analyzing urban dynamics and land-use transitions.

The 30-year LULC time series indicates sustained and intensive urbanization in Ha Long City, evidenced by a substantial expansion of built-up land and a rise in the regional urbanization rate from 8.7% in 1995 to nearly 30% in 2025. Urban growth has concentrated along coastal and bayfront areas, and major transportation corridors, while natural forest, mangrove forest, and surface water have declined markedly. These changes highlight the role of large-scale land reclamation in Cua Luc Bay and Ha Long Bay in shaping recent urban development.

Analysis of urbanization rate and intensity shows contrasts between areas where buildable land is nearly saturated and regions that retain expansion potential. Areas with high urbanization speed but low urbanization intensity represent potential future growth centers, whereas zones approaching saturation indicate tendencies toward vertical development or outward expansion into peri-urban regions. Using these two metrics derived from the LULC maps enables a comprehensive assessment of land-conversion dynamics and quantification of remaining land capacity for urban development. This approach provides valuable information to support planning policies and guide sustainable development strategies for Ha Long in the coming decades.

## Acknowledgement

The authors would like to thank the United States Geological Survey (USGS) and the European

Space Agency (ESA) for providing access to the remote sensing datasets used in this study. This research was supported by the Hanoi University of Civil Engineering under the institutional research project “20-2023/KHXD-TĐ”.

## Contributions of authors

Hung Manh Nguyen: investigation, formal analysis, data curation, visualization. Toan Duy Dao: conceptualization, methodology, formal analysis, writing – original draft, project administration. Chieu Dinh Vu: writing – original draft. Dung Ngoc Luong: writing – original draft. Dong Thanh Khuc: methodology, validation, writing – review and editing. Son Mai Le: data curation, resources. Trong Gia Nguyen: supervision, writing – review and editing.

## References

Belgiu, M., & Drăguţ, L. (2016). Random forest in remote sensing: A review of applications and future directions. *ISPRS Journal of Photogrammetry and Remote Sensing*, 114: 24-31.

Breiman, L. (2001). Random Forests. *Machine Learning*, 45(1): 5-32.

Brown, C. F., Brumby, S. P., Guzder-Williams, B., Birch, T., Hyde, S. B., Mazzariello, J., Czerwinski, W., Pasquarella, V. J., Haertel, R., & Ilyushchenko, S. (2022). Dynamic World, Near real-time global 10 m land use land cover mapping. *Scientific Data*, 9(1): 251.

Cao, A., Esteban, M., Onuki, M., Nguyen, K., Nguyen, D. T., & Le, V. T. (2021). Decoupled formal and informal flooding adaptation and conflicts in coastal cities: A case study of Ho Chi Minh City. *Ocean & Coastal Management*, 209: 105654.

Castrence, M., Nong, D. H., Tran, C. C., Young, L., & Fox, J. (2014). Mapping Urban Transitions Using Multi-Temporal Landsat and DMSP-OLS Night-Time Lights Imagery of the Red River Delta in Vietnam. *Land*, 3: 148-166. DOI: 10.3390/land3010148.

Dang, T. T., Nguyen, T. T, Hoang, T. T., Ta, M. N., Dinh, T. T. H., & Pham, L. C. (2023). Analyzing Urban Expansion in Hanoi Using Machine Learning and Multi-Temporal Satellite Imagery. *International Conference on Geoinformatics for Spatial-Infrastructure Development in Earth & Allied Sciences*, Springer.

Destefanis, T., Guliyeva, S., Boccardo, P., & Fissore, V. (2025). Advancing Flood Detection and Mapping: A Review of Earth Observation Services, 3D Data Integration, and AI-Based Techniques. *Remote Sensing*, 17: 2943.

Do, T. T. H., Tran, D. L., Nguyen, T. T. H., Nguyen, D. V., & Nguyen, V. T. (2025). Application of GIS and remote sensing in detecting coastal reclamation in the coastal areas of Hai Phong-Ha Long from 1990 to 2020. *Vietnam Journal of Marine Science Technology*, 25(1): 29-39.

Duong, L. T., Dang, K. V., Dao, N. H., Nguyen, T. D., Dinh, X. V., & Weber, C. (2021). Monitoring of coastline change using Sentinel-2A and Landsat 8 data, a case study of Cam Pha city-Quang Ninh province. *Vietnam Journal of Earth Sciences*, 43(3): 249-272.

Feyisa, G. L., Meilby, H., Fensholt, R., & Proud, S. R. (2014). Automated Water Extraction Index: A new technique for surface water mapping using Landsat imagery. *Remote Sensing of Environment*, 140: 23-35.

Foody, G. M. (2002). Status of land cover classification accuracy assessment. *Remote Sensing of Environment*, 80(1): 185-201.

Foody, G. M. (2020). Explaining the unsuitability of the kappa coefficient in the assessment and comparison of the accuracy of thematic maps obtained by image classification. *Remote Sensing of Environment*, 239: 111630.

Goldblatt, R., Deininger, K., & Hanson, G. (2018). Utilizing publicly available satellite data for urban research: Mapping built-up land cover and land use in Ho Chi Minh City, Vietnam. *Development Engineering*, 3: 83-99.

Goutte, C., & Gaussier, E. (2005). A probabilistic interpretation of precision, recall and F-score, with implication for evaluation. *European Conference on Information Retrieval*, Springer.

Gupta, K., Mukhopadhyay, A., Giri, S., Chanda, A., Majumdar, S., Samanta, S., Mitra, D., Samal, D. R., Pattnaik, A., & Hazra, S. (2018). An Index for discrimination of mangroves from non-mangroves using Landsat 8 OLI imagery. *MethodsX*, 5.

Hinkel, J., Lincke, D., Vafeidis, A. T., Perrette, M., Nicholls, R. J., Tol, R. S., Marzeion, B., Fettweis, X., Ionescu, C., & Levermann, A. (2014). Coastal flood damage and adaptation costs under 21st century sea-level rise. *PNAS*, 111(9): 3292-3297.

Jalilov, S., Chen, Y., Quang, N., Nguyen, M., Leighton, B., Paget, M., & Lazarow, N. (2021). Estimation of Urban Land-Use Efficiency for Sustainable Development by Integrating over 30-Year Landsat Imagery with Population Data: A Case Study of Ha Long, Vietnam. *Sustainability*, 13: 8848.

Kirezci, E., Young, I. R., Ranasinghe, R., Lincke, D., & Hinkel, J. (2023). Global-scale analysis of socioeconomic impacts of coastal flooding over the 21st century. *Frontiers in Marine Science*, 9: 1024111.

Ma, L., Liu, Y., Zhang, X., Ye, Y., Yin, G., & Johnson, B. A. (2019). Deep learning in remote sensing applications: A meta-analysis and review. *ISPRS Journal of Photogrammetry Remote Sensing*, 152: 166-177.

Mauro, G. (2020). Rural-urban transition of Hanoi (Vietnam): Using Landsat imagery to map its recent peri-urbanization. *ISPRS International Journal of Geo-Information,* 9(11): 669.

Mishra, A., Agnihotri, A. K., Pipil, S., Gaur, S., & Ohri, A. (2024). Chapter 4 - Surveying techniques for urban areas. *In Earth Observation in Urban Monitoring*. Elsevier: 69-91.

Ngo, V. L., Dang, V. B., Dang, K. B., Ngo, C. C., Pham, T. P. N., Burkhard, B., & Giap, T. K. C. (2020). Assessment of shoreline changes for setback zone establishment from Son Tra (Da Nang city) to Cua Dai (Hoi An city), Vietnam. *Vietnam Journal of Earth Sciences*, 42(4): 363-383.

Nguyen, D. D., Nierynck, E., Tran, V. Y., & Hens, L. (2000). Land Use Changes and GIS-database Development for Strategic Environmental Assessment in Ha Long Bay, Quang Ninh Province, Vietnam. *Application of Resource Information Technologies (GIS/GPS/RS) in Forest Land and Resources Management*, Hanoi, Vietnam.

Nguyen, H. T. T., & Chinh, V. D. (2025). Rehabilitation of Mangrove Ecosystem for Hai Phong Coastal Protection. *Proceedings of the 3rd Vietnam Symposium on Advances in Offshore Engineering*, Singapore, Springer Nature Singapore.

Nguyen, M. T., Sebesvari, Z., Souvignet, M., Bachofer, F., Braun, A., Garschagen, M., Schinkel, U., Yang, L. E., Nguyen, L. H. K., Hochschild, V., Assmann, A., & Hagenlocher, M. (2021). Understanding and assessing flood risk in Vietnam: Current status, persisting gaps, and future directions. *Journal of Flood Risk Management*, 14(2): e12689.

Nong, D. H., Fox, J., Miura, T., & Saksena, S. (2015). Built-up Area Change Analysis in Hanoi Using Support Vector Machine Classification of Landsat Multi-Temporal Image Stacks and Population Data. *Land*, 4: 1213-1231. DOI: 10.3390/land4041213.

Pham, S. H., Bui, T. M. H., & La, V. T. (2023). Vulnerability and Flood Risk Analysis for Urban Areas—A Case Study of Ho Chi Minh City. In *Urban Transformational Landscapes in the City-Hinterlands of Asia*. Springer Nature Singapore: 345-358.

Pham, T. B., Le, D. M., Tran, T. H., Tran, V. B., Lau, V. K., & Nguyen, H. H. (2025). Change of Coastline and Beach of Nha Trang Bay. *In Russian-Vietnamese Oceanographic Research in the South China Sea*. Springer Nature Switzerland: 241-263.

Rasul, A., Balzter, H., Smith, C., Remedios, J., Adamu, B., Sobrino, J. A., Srivanit, M., & Weng, Q. (2017). A review on remote sensing of urban heat and cool islands. *Land*, 6(2): 38.

Reimann, L., Vafeidis, A. T., & Honsel, L. E. (2023). Population development as a driver of coastal risk: Current trends and future pathways. Cambridge Prisms: *Coastal Futures*, 1: e14.

Rouse, J. W. (1973). Monitoring vegetation systems in the Great Plains with ERTS. *Third NASA Earth Resources Technology Satellite Symposium*.

Tran, V. T., Dinh, V. D., Lam, T. P., Huynh, V. M., Nguyen, T. T., Nguyen, T. U., & Downes, N. K. (2024). Coastal Erosion Dynamics and Protective Measures in the Vietnamese Mekong Delta. *Journal of Marine Science and Engineering*, 12: 1094. DOI: 10.3390/jmse12071094.

Trinh, T. H. T. & Bui, T. H. T. (2023). Study of the urban heat island intensity using Landsat 8 in Da Nang in 2020. *Journal of Mining Earth Sciences*, 64(3): 79-89.

United Nations (UN) (2011). Percentage of total population living in coastal areas. *Socioeconomic Data and Applications Center*, Columbia, SC, USA.

Vachaud, G., Quertamp, F., Phan, T. S. H., Ngoc, T. D. T., Nguyen, T., Luu, X. L., Nguyen, A. T., & Gratiot, N. (2019). Flood-related risks in Ho Chi Minh City and ways of mitigation. *Journal of Hydrology*, 573: 1021-1027.

Van Maren, D., Schrijvershof, R., Beemster, J., Zhu, C., Xie, D., Zhou, Z., Colina Alonso, A., & Hoitink, A. (2025). Land reclamation impacts on tidal landscape evolution. *Reviews of Geophysics*, 63(3): e2024RG000860.

Vu, T. A., Ngo, A. D., Nguyen, H. P. T., & Nguyen, G. C. (2024). Applying object-based approach to monitor urban expansion in Ha Long city, Vietnam, during 2000-2023 from multi-date Landsat satellite imagery. *European Journal of Remote Sensing*, 57.

World Bank (WB). (2025). Living or Leaving: Life in the Mekong Delta Region of Viet Nam.

Wulder, M. A., Loveland, T. R., Roy, D. P., Crawford, C. J., Masek, J. G., Woodcock, C. E., Allen, R. G., Anderson, M. C., Belward, A. S., & Cohen, W. B. (2019). Current status of Landsat program, science, and applications. *Remote Sensing of Environment*, 225: 127-147.

Xiao, H., Tang, Y., Li, H., Zhang, L., Ngo-Duc, T., Chen, D., & Tang, Q. (2021). Saltwater intrusion into groundwater systems in the Mekong Delta and links to global change. *Advances in Climate Change Research*, 12(3): 342-352.

Xu, H. (2006). Modification of normalised difference water index (NDWI) to enhance open water features in remotely sensed imagery. *International Journal of Remote Sensing*, 27(14): 3025-3033.

Zha, Y., Gao, J., & Ni, S. (2003). Use of normalized difference built-up index in automatically mapping urban areas from TM imagery. *International Journal of Remote Sensing,* 24(3): 583-594.

Zhou, Y., & Weng, Q. (2024). Building up a data engine for global urban mapping. *Remote Sensing of Environment*, 311: 114242.

Zhu, X. X., Tuia, D., Mou, L., Xia, G.-S., Zhang, L., Xu, F., & Fraundorfer, F. (2017). Deep learning in remote sensing: A comprehensive review and list of resources. *IEEE Geoscience Remote Sensing Magazine*, 5(4): 8-36.